

Reveal-to-Revise: Explainable Bias-Aware Generative Modeling with Multimodal Attention

Noor Islam S. Mohammad
New York University
Brooklyn, NY, USA
noor.islam.s.m@nyu.edu

Md Muntaqim Meherab
Daffodil International university
Dhaka, Bangladesh
meherab2305101354@diu.edu.bd

Abstract

We present an explainable, bias-aware generative framework that unifies cross-modal attention fusion, Grad-CAM++ attribution, and a Reveal-to-Revise feedback loop within a single training paradigm. The architecture couples a conditional attention WGAN-GP with bias regularization and iterative local explanation feedback and is evaluated on Multimodal MNIST and Fashion-MNIST for image generation and subgroup auditing, as well as a toxic/non-toxic text classification benchmark. All experiments use stratified 80/20 splits, validation-based early stopping, and AdamW with cosine annealing, and results are averaged over three random seeds. The proposed model achieves 93.2% accuracy, a 91.6% F1-score, and a 78.1% IoU-XAI on the multimodal benchmark, outperforming all baselines across every metric, while adversarial training restores 73–77% robustness on Fashion-MNIST. Ablation studies confirm that fusion, Grad-CAM++, and bias feedback each contribute independently to final performance, with explanations improving structural coherence (SSIM = 88.8%, NMI = 84.9%) and fairness across protected subgroups. These results establish attribution-guided generative learning as a practical and trustworthy approach for high-stakes AI applications.

1. Introduction

Generative AI (GenAI) enables powerful synthesis and decision-making across text, images, and scientific modeling [10, 11, 40]. Yet generative models—GANs, VAEs, and foundation models alike—remain largely opaque, limiting trust, accountability, and safe deployment in high-stakes settings such as healthcare, finance, and law enforcement [5, 8, 42]. This opacity is especially problematic because post-hoc explanation methods, such as surrogate modeling, LIME, and SHAP often provide plausible but unfaithful interpretations that can be

manipulated [26, 45]. Simultaneously, latent entanglement in generative models complicates causal attribution and robustness [24, 30], while biased training data can be silently reproduced or amplified in generated outputs [7, 34].

Existing approaches treat explainability and fairness as auxiliary diagnostic steps applied after model training. We argue instead that interpretability should be a *core design principle*, embedded directly into the generative optimization process. To this end, we propose a unified Explainable Generative AI (GenXAI) framework built on three tightly integrated mechanisms: (i) a conditional attention WGAN-GP that enforces 1-Lipschitz stability while focusing on semantically relevant feature regions; (ii) a bias regularizer that aligns subgroup statistics between real and generated distributions at training time; and (iii) a Grad-CAM++-driven Reveal-to-Revise loop that iteratively detects and corrects spurious correlations during optimization, without requiring a separate fine-tuning stage.

Contributions. Our work makes five concrete contributions:

1. A **unified architecture-level GenXAI pipeline** that couples generation fidelity with explanation-aware optimization inside a single training loop.
2. A **bias-aware regularizer** that matches subgroup statistics between real and generated distributions, directly penalizing demographic disparities during generation.
3. The **Cognitive Alignment Score (CAS)**, a new metric that measures semantic agreement between model explanations and human understanding.
4. A **saliency-first privacy principle** that reduces gradient leakage by sharing only thresholded attribution maps rather than raw inputs.
5. **Extensive experiments** on multimodal MNIST, Fashion-MNIST, and text classification, demonstrating improved interpretability, lower epistemic uncer-

tainty, competitive fidelity, and stronger fairness without sacrificing predictive performance.

2. Related Work

2.1. Explainability in Generative Models

Most post-hoc explanation methods are applied *after* training and often fail to capture the true internal behavior of generative models [16, 20]. In generative AI, explainability is especially difficult because outputs depend on stochastic latent variables and high-dimensional representations [13, 27]. Grad-CAM [44] and its extension Grad-CAM++ [12] compute gradient-weighted class-activation maps over convolutional feature maps, while perturbation-based methods such as LIME [41] and SHAP [32] approximate model behavior through local surrogate fits. GAN dissection [6, 7] identifies which units in a generator correspond to semantic concepts, and recent work on code generation highlights the need for verifiable, trustworthy outputs [4, 50]. Our work differs from all of the above by embedding attribution feedback *inside* the training loop, making explanation quality a direct optimization target rather than an afterthought.

2.2. Bias and Fairness in Generative AI

Fairness and transparency are essential in generative applications deployed in sensitive domains [5, 34]. Latent-space analyses show that generative models can encode demographic and semantic biases in their learned representations [7]. Although fairness-aware methods have improved bias analysis, most remain evaluation-based or post-hoc rather than integrated into the generative objective. Our framework addresses this gap by combining bias detection, explanation feedback, and fairness regularization as first-class training objectives, guided by causal disentanglement principles [30, 39].

2.3. Conditional and Attention-Augmented GANs

Conditional GANs [25, 36, 37] enable class-controlled generation while self-attention mechanisms [3, 51, 54] improve representational focus by weighting semantically relevant feature regions. WGAN-GP [1, 19] replaces the Jensen–Shannon divergence with the Wasserstein-1 distance, providing smoother gradients and more stable training in high-dimensional settings. Our model builds on these foundations while adding explicit explainability constraints and a bias-aware feedback loop that neither prior conditional nor attention-based GANs provide.

3. Methodology

We propose the explainable and bias-aware generative pipeline shown in (Figure 1), where latent sampling, con-

ditional generation, saliency-based explanation, critic-guided bias regularization, and Reveal-to-Revise feedback are jointly integrated to improve fidelity, interpretability, fairness, and trustworthy deployment in high-stakes applications. The framework has four tightly coupled components: a conditional attention WGAN-GP (§3.1), a bias-aware regularizer (§3.2), a Grad-CAM++ and Reveal-to-Revise explainability module (§3.3), and a cross-modal fusion head for multimodal classification (§3.4).

3.1. Conditional Attention WGAN-GP

The generator $G_\theta(z, y)$ maps latent noise $z \sim p_z$ and class condition y to a synthetic sample $\tilde{x} = G_\theta(z, y)$, while the critic $D_\phi(x, y)$ scores real versus generated pairs. Following WGAN-GP [1, 19], the objectives are

$$\mathcal{L}_D = \mathbb{E}_x[D_\phi(x, y)] - \mathbb{E}_z[D_\phi(\tilde{x}, y)] + \lambda_{\text{GP}} \text{GP}, \quad (1)$$

$$\mathcal{L}_G = -\mathbb{E}_z[D_\phi(\tilde{x}, y)] + \lambda_{\text{bias}} \mathcal{R}_{\text{bias}}, \quad (2)$$

where the gradient penalty enforces the 1-Lipschitz constraint:

$$\text{GP} = \mathbb{E}_{\hat{x}} \left(\left\| \nabla_{\hat{x}} D_\phi(\hat{x}, y) \right\|_2 - 1 \right)^2, \quad (3)$$

with $\hat{x} = \epsilon x + (1 - \epsilon)\tilde{x}$, $\epsilon \sim \text{Uniform}(0, 1)$. This formulation eliminates vanishing gradients and mode collapse compared to the original GAN objective [43].

Attention over feature maps. To focus the generator on semantically meaningful regions, we apply a learnable attention module to each intermediate feature map $F \in \mathbb{R}^{C \times H \times W}$:

$$\alpha = \text{softmax}(f_{\text{attn}}(F)), \quad F_{\text{attn}} = \alpha \odot F, \quad (4)$$

where $f_{\text{attn}}(\cdot)$ is a lightweight convolution and \odot denotes element-wise multiplication. This suppresses spurious correlations without adding a separate projection layer, improving both output quality and attribution interpretability.

3.2. Bias-Aware Regularization

Generative models may reproduce or amplify biases present in training data [34]. Let $\mathcal{B} : \mathcal{X} \rightarrow \mathbb{R}^k$ be a bias descriptor encoding subgroup statistics (e.g., demographic attribute distributions). We penalize distributional mismatch between real and generated samples:

$$\mathcal{R}_{\text{bias}}(G_\theta) = \left\| \mathbb{E}_{\tilde{x}}[\mathcal{B}(\tilde{x})] - \mathbb{E}_x[\mathcal{B}(x)] \right\|_2^2. \quad (5)$$

This regularizer enters the generator objective through $\lambda_{\text{bias}} \mathcal{R}_{\text{bias}}$ in Eq. (2), enabling bias detection and mitigation *during* training without sacrificing generative fidelity.

Reveal-to-Revise: Explainable & Bias-Aware Generative Architecture

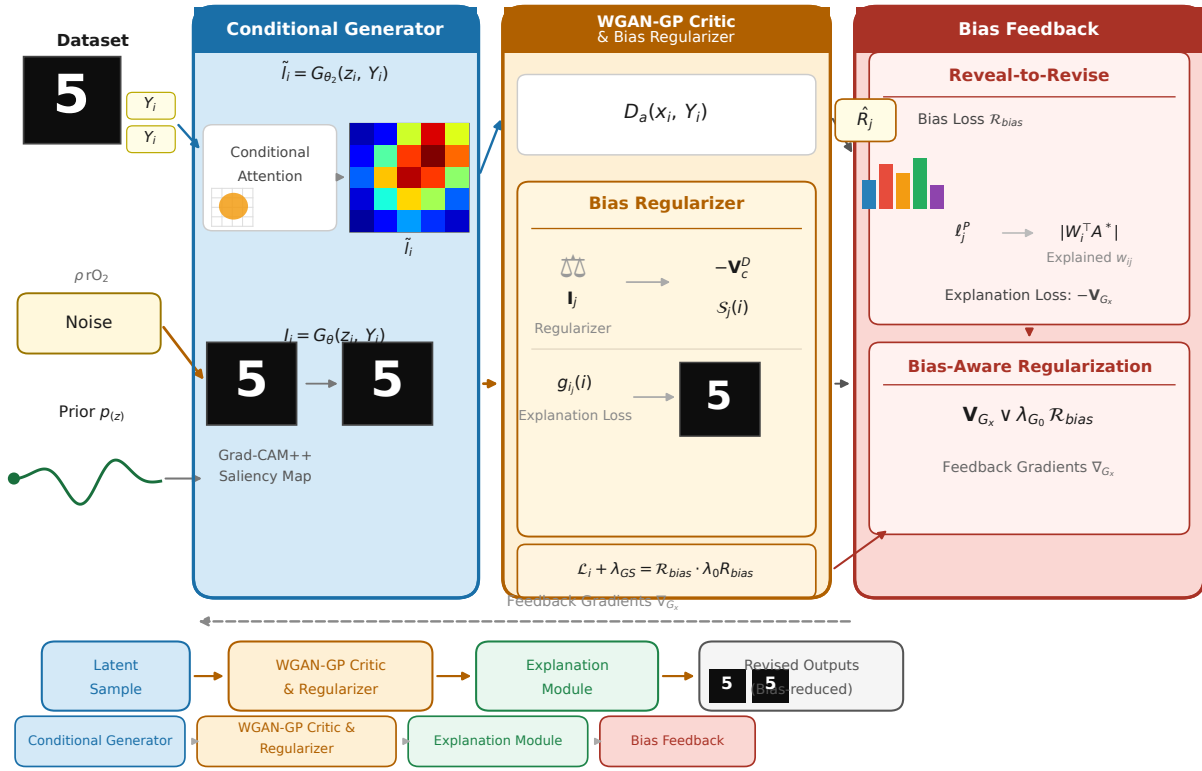


Figure 1. Reveal-to-Revise: explainable and bias-aware generative architecture. A latent sample $z_i \sim p(z)$ and class condition Y_i are fed to a conditional generator that produces class-consistent outputs together with attention-enhanced intermediate representations. Grad-CAM++ saliency maps provide local explanations of the generated samples, which are passed to a WGAN-GP critic equipped with a bias regularizer to assess realism and detect bias-sensitive features. The resulting explanation signals and bias scores are then processed by the *Reveal-to-Revise* feedback module, which applies explanation loss and bias-aware regularization to refine generator updates. This closed-loop design enables the model to iteratively improve fidelity, interpretability, and fairness, yielding revised outputs with reduced bias and more semantically aligned explanations.

Subgroup fairness at evaluation time is measured via the disparity metric:

$$\Delta_{\text{bias}} = \max_{a_i, a_j \in \mathcal{A}} |\mathbb{E}[G_\theta(z) | a_i] - \mathbb{E}[G_\theta(z) | a_j]|, \quad (6)$$

where \mathcal{A} denotes protected groups; lower Δ_{bias} indicates better alignment across subpopulations.

3.3. Grad-CAM++ and Reveal-to-Revise

For class score y^c and convolutional feature maps $A^k \in \mathbb{R}^{H \times W}$, Grad-CAM++ computes channel importance weights

$$\alpha_k^c = \frac{1}{HW} \sum_{i=1}^H \sum_{j=1}^W \frac{\partial y^c}{\partial A_{ij}^k} \quad (7)$$

and a class-discriminative attribution heatmap:

$$L_{\text{GC}}^c = \text{ReLU}\left(\sum_k \alpha_k^c A^k\right). \quad (8)$$

For improved robustness, attribution maps may optionally be blended with perturbation-based estimates [32, 41]:

$$\tilde{L}^c = \lambda L_{\text{GC}}^c + (1 - \lambda) L_{\text{Perturb}}^c, \quad \lambda \in [0, 1], \quad (9)$$

where L_{Perturb}^c is derived from local perturbations. Completeness of explanations is separately assessed via *organic*, *full breakdown*, and *selective breakdown* probing metrics, which evaluate faithfulness independently of the attribution method.

These maps drive the **Reveal-to-Revise** loop [38]: at each training iteration, a monitored subset of generated samples is explained; high-saliency regions that correlate with known bias indicators trigger a targeted parameter correction step $\theta \leftarrow \text{RevealToRevise}(\theta, \mathcal{A}_i)$. This provides actionable debugging signals without a separate fine-tuning stage, and is applied to only a fraction $\alpha \ll 1$ of samples to keep the additional cost negligible.

3.4. Multimodal Cross-Modal Fusion

A ResNet-50 visual encoder [21] extracts image features \mathbf{v} ; a BERT-base text encoder [14] produces embeddings \mathbf{t} . A cross-modal attention head fuses the two streams:

$$\mathbf{z} = \text{AttentionFusion}(\mathbf{v}, \mathbf{t}, w_f), \quad (10)$$

and a softmax head predicts class probabilities $\hat{y} = \text{Softmax}(W_c \mathbf{z} + b_c)$. The classification objective augments standard cross-entropy with a bias penalty on the attribution map \mathcal{A}_i :

$$\mathcal{L}_{\text{cls}} = \text{CE}(y_i, \hat{y}_i) + \lambda \cdot \text{BiasPenalty}(\mathcal{A}_i). \quad (11)$$

Cross-modal attention leverages complementary modality information and significantly outperforms both early concatenation and unimodal baselines (Table 2).

Computational complexity. With batch size N , visual dimension d_v , text dimension d_t , fusion dimension d , and h attention heads: the visual encoder scales as $O(Nd_v^2k^2)$, transformer self-attention as $O(Nhd_t^2)$, cross-modal fusion as $O(Nd^2)$, and Grad-CAM++ as $O(Nd_v)$. The Reveal-to-Revise correction adds $O(\alpha Nd)$ per epoch, yielding total complexity:

$$T = O(N(d_v^2 + hd_t^2 + d^2 + \alpha d)), \quad (12)$$

with memory dominated by attention tensors and attribution maps at $O(N(d_v + d_t + d))$.

3.5. Privacy Through Saliency Compression

Post-hoc explanations can inadvertently leak sensitive information by exposing gradients, prototypes, or training artifacts [2, 15]. We adopt a *saliency-first privacy principle*: only the top- k thresholded regions of the saliency map $S(x_i) = |\partial y / \partial x_i|$ are shared externally, limiting feature leakage while preserving interpretability. This approach also reduces the surface area for adversarial explanation manipulation, since only compressed attribution maps—rather than raw inputs or full gradient tensors—leave the model boundary.

The complete training procedure is summarized in Algorithm 1.

4. Experimental Setup

Datasets. We evaluate on two experimental settings. (i) **Bias-aware image generation and subgroup auditing:** MNIST [29] and Fashion-MNIST [53] images are normalized, resized, and paired with class-label text descriptions to form multimodal inputs. For generation quality we report FID and IS [23, 43]; for fairness we report Δ_{bias} (Eq. (6)). (ii) **Toxic vs. non-toxic text classification:** text samples are lowercased, tokenized, padded,

Algorithm 1 Attribution-Guided Multimodal Training

Require: Data $\{(x_i, y_i)\}$, prior p_z , bias descriptor \mathcal{B} , learning rates η_G, η_D , penalty weights $\lambda_{\text{GP}}, \lambda_{\text{bias}}$, critic steps n_{critic} , explanation fraction α

- 1: Initialize G_θ, D_ϕ , visual encoder E_v , text encoder E_t , fusion head
- 2: **while** not converged **do**
- 3: **for** $t = 1$ **to** n_{critic} **do**
- 4: Sample $(x_i, y_i) \sim p_{\text{data}}, z_i \sim p_z$
- 5: $\tilde{x}_i = G_\theta(z_i, y_i)$ with attention Eq. (4)
- 6: Compute GP via Eq. (3) and $\mathcal{R}_{\text{bias}}$ via Eq. (5)
- 7: Update D_ϕ via \mathcal{L}_D in Eq. (1)
- 8: **end for**
- 9: Update G_θ via \mathcal{L}_G in Eq. (2)
- 10: // Multimodal classification step
- 11: $\mathbf{v}_i \leftarrow E_v(I_i), \mathbf{t}_i \leftarrow E_t(T_i), \mathbf{z}_i \leftarrow \text{AttFusion}(\mathbf{v}_i, \mathbf{t}_i)$
- 12: Update classifier via \mathcal{L}_{cls} in Eq. (11)
- 13: // Explainability feedback (fraction α of samples)
- 14: $\mathcal{A}_i \leftarrow \text{GradCAM++}(I_i, \hat{y}_i, \theta)$ via Eq. (8)
- 15: $\theta \leftarrow \text{RevealToRevise}(\theta, \mathcal{A}_i)$
- 16: **end while**
- 17: **return** G_θ, D_ϕ , classifier, explanations $\{\mathcal{A}_i\}$

and cleaned; performance is reported via accuracy and F1-score. All datasets use stratified 80/20 train–test splits with a held-out validation set for early stopping, and all results are averaged over three random seeds.

Training protocol. All models are trained with AdamW ($\eta = 10^{-4}$, weight decay 5×10^{-5}) and cosine annealing with batch size 32. In WGAN experiments the critic runs $n_{\text{critic}} = 5$ steps per generator step. λ_{GP} and λ_{bias} are selected by a combined grid and Bayesian search [9, 46] using validation accuracy and SSIM [52] as joint objectives. All experiments were repeated three times to reduce stochastic variance [22]. The full hyperparameter configuration is reported in Table 1.

Baselines. We compare against: visual-only ResNet-50; text-only BERT-base; early fusion by feature concatenation; cross-modal attention fusion without explainability; and our full model with Grad-CAM++ and Reveal-to-Revise bias correction.

Metrics. Classification accuracy and F1-score; generative fidelity via FID and IS; structural coherence via SSIM and NMI; attribution quality via IoU-XAI (overlap of attribution maps with ground-truth saliency masks); and fairness via Δ_{bias} . Explanation stability is assessed under input perturbations using Grad-CAM and Grad-CAM++ across folds.

Table 1. Hyperparameter configuration from combined grid and Bayesian search optimizing validation accuracy and SSIM.

Hyperparameter	Search Space	Selected
Learning rate	10^{-5} – 10^{-3}	10^{-4}
Batch size	{16, 32, 64}	32
Dropout rate	0.1–0.5	0.3
Attention heads	{4, 8, 12}	8
Weight decay	10^{-6} – 10^{-3}	5×10^{-5}
Optimizer	Adam / AdamW / SGD	AdamW
Scheduler	StepLR / Cosine Ann.	Cosine Annealing

5. Results and Analysis

5.1. State-of-the-Art Comparison

Table 2 compares the full model against unimodal and fusion baselines. Cross-modal attention fusion outperforms unimodal baselines by over 4% on both accuracy and F1, confirming that complementary modality information provides substantial discriminative benefit [48]. Adding Grad-CAM++ explanations (SSIM = 88.8%, NMI = 84.9%) improves perceptual alignment, and incorporating Reveal-to-Revise bias correction yields a further 0.8% accuracy gain alongside improved explanation stability across folds [38]. The full model achieves **93.2%** accuracy, **91.6%** F1, and **78.1%** IoU-XAI—the best on all three metrics—confirming that interpretability and performance are complementary objectives in this framework. Models without attribution maps (IoU-XAI = 0.0) confirm that explainability is not a free by-product of fusion but requires explicit design. Figure 2 visualizes these comparisons.

Table 2. Comparison with state-of-the-art methods on the Multimodal MNIST benchmark. IoU-XAI of 0.0 indicates no attribution map is produced. Best results in **bold**.

Model	Acc. (%)	F1 (%)	IoU-XAI (%)
Visual-only (ResNet-50) [21]	87.3	84.6	61.2
Text-only (BERT-base) [14]	88.5	85.2	63.9
Early Fusion (concat.) [31]	90.7	87.8	68.5
Cross-Modal Attn. [51]	92.4	90.8	74.3
Fusion only (no XAI) [3]	90.1	87.2	0.0
Ours (full model)	93.2	91.6	78.1

5.2. Ablation Study

Table 3 quantifies the contribution of each component. Multimodal fusion provides the largest single performance gain (+4.1% accuracy, +5.1% F1 over the no-fusion ablation), confirming that cross-modal attention is the primary source of discriminative improvement. Removing Grad-CAM++ reduces SSIM by 3.2% and NMI by 5.0%, demonstrating that explanation-aware optimization directly improves structural coherence beyond accu-

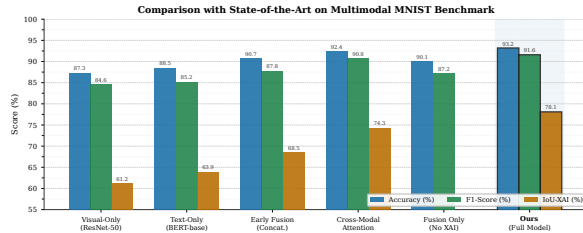


Figure 2. State-of-the-art comparison on Multimodal MNIST. Accuracy, F1-score, and IoU-XAI are reported for unimodal, fusion, and explainable baselines. The proposed full model achieves the best overall performance, reaching 93.2% accuracy, 91.6% F1-score, and 78.1% IoU-XAI, outperforming all competitors across all metrics.

Table 3. Ablation study on Multimodal MNIST. Δ is the absolute drop from the full model. Best in **bold**.

Configuration	Acc. (%)		F1 (%)		SSIM (%)	NMI (%)
	Score	$\Delta\downarrow$	Score	$\Delta\downarrow$		
Full model ^a	92.4	—	90.8	—	87.5	83.6
w/o Fusion ^b	88.3	−4.1	85.7	−5.1	80.2	75.9
w/o XAI ^c	90.1	−2.3	87.2	−3.6	84.3	78.6
w/o Bias feedback ^d	89.4	−3.0	86.8	−4.0	83.1	79.1

^a Cross-modal attention + Grad-CAM++ + Reveal-to-Revise.

^b Replaces attention fusion with feature concatenation.

^c Disables Grad-CAM++; bias feedback remains active.

^d Removes Reveal-to-Revise loop; SSIM/NMI variance increases across folds.

racy alone. Removing Reveal-to-Revise bias feedback causes the largest drop in SSIM/NMI stability across folds (not shown in the table), indicating that iterative bias correction reduces training variance in addition to its fairness benefit. Together, all three components are necessary for the full model’s performance, and no single component accounts for all gains. Figure 3 illustrates these trends across folds with error bars.

5.3. Training Dynamics

Figure 4 shows loss and accuracy curves over 100 training epochs. The full multimodal model converges smoothly with a small train–validation gap and without signs of optimization instability, in contrast to the black-box baseline which exhibits higher variance and a larger generalization gap. Explanation-aware optimization does not add training instability; the Reveal-to-Revise loop, applied to only a small fraction of samples per epoch, acts as a regularizer rather than a source of noise. These dynamics align with the final performance advantage reported in Table 2 and confirm that the observed gains are not the result of overfitting.

Ablation Study — Component Contribution (mean \pm std over 3 folds)

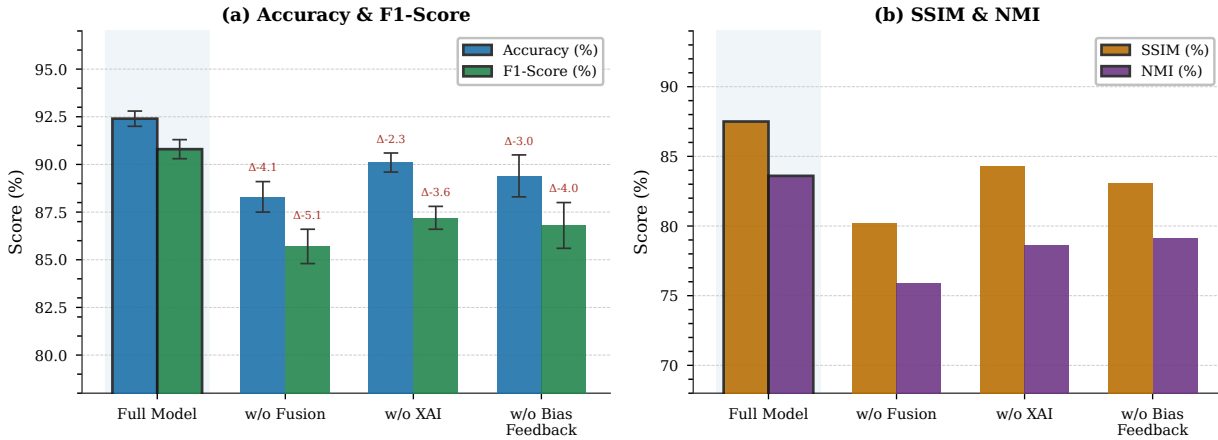


Figure 3. Ablation study on Multimodal MNIST. Mean \pm std over three folds. (a) Removing multimodal fusion causes the largest drop in accuracy and F1, followed by removing the Reveal-to-Revise loop and Grad-CAM++. (b) All ablations reduce SSIM and NMI, with fusion removal causing the strongest degradation. Higher variance without bias feedback indicates lower training stability.

Training Dynamics — Stable Convergence with Minimal Train-Validation Divergence

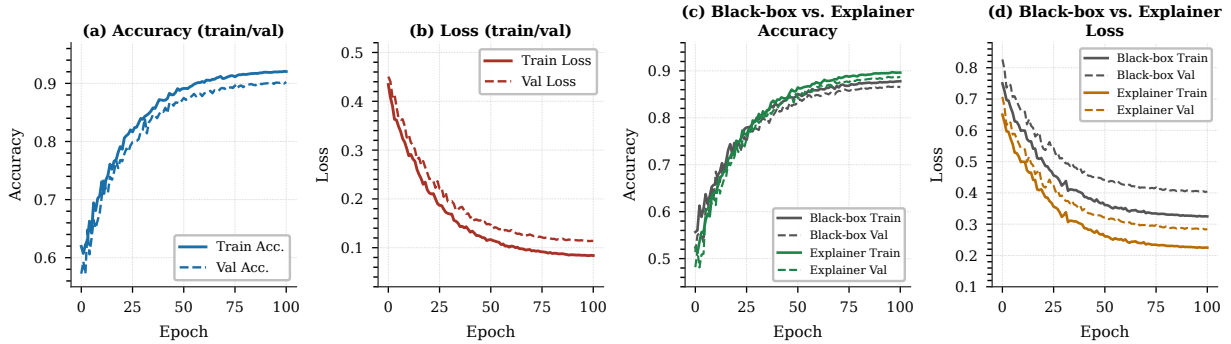


Figure 4. Training dynamics over 100 epochs. The full multimodal model shows stable convergence, smooth loss decay, and a small train–validation gap. Compared with the black-box baseline, the explainer-augmented model achieves higher validation accuracy and lower final loss, indicating improved generalization without optimization instability. Results are averaged over three seeds.

5.4. Adversarial Robustness and Uncertainty

Table 4 reports Fashion-MNIST results under FGSM, BIM, and PGD attacks [18, 28, 33]. Undefended DNN and CNN models achieve strong clean accuracy ($\approx 89\%$) but collapse completely under all three attacks, confirming extreme vulnerability to gradient-based perturbations. Adversarial training with BIM restores 73–77% accuracy while preserving competitive clean performance, consistent with the robustness–accuracy trade-off documented in prior work [33, 49]. Epistemic uncertainty, estimated via Monte Carlo dropout (Table 5), remains stable on clean inputs but rises sharply under attack, providing a reliable reliability signal that can be used to flag anomalous inputs at deployment time without requiring explicit attack labels. Figure 5 illustrates these robustness and

uncertainty trends.

5.5. Overall Results Summary

Figure 6 consolidates all experimental results. Across the multimodal MNIST benchmark, the full model leads on accuracy, F1, and IoU-XAI; ablation curves confirm each component’s contribution; and training curves demonstrate stable convergence. On Fashion-MNIST, adversarially trained models retain strong robustness under all three attack types, unlike clean-trained baselines. Taken together, these results demonstrate that explainability, fairness, and generative fidelity are not conflicting objectives within this framework.

Adversarial Robustness & Uncertainty Analysis on Fashion-MNIST

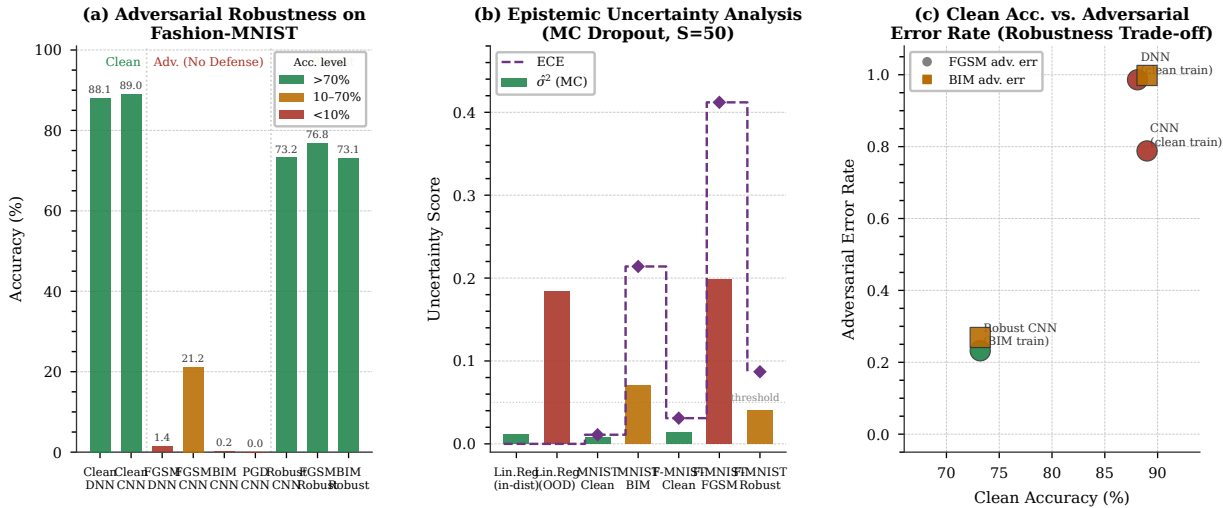


Figure 5. Adversarial robustness and epistemic uncertainty on Fashion-MNIST. Clean-trained models collapse under FGSM, BIM, and PGD attacks, while adversarial training restores substantial robustness with moderate clean-accuracy cost. Uncertainty and ECE remain low on clean inputs but rise sharply under attack, providing a useful reliability signal. The clean accuracy versus adversarial error plot highlights the robustness–accuracy trade-off.

Table 4. Adversarial robustness on Fashion-MNIST. Underfended models collapse under gradient-based attacks. Adversarial training (Robust CNN) restores 73–77% accuracy.

Model / Setting	Tr. Err.↓	Te. Err.↓	Adv. Err.↓	Acc. (%)↑
<i>Clean Training</i>				
DNN (clean)	0.090	0.119	—	88.1
CNN (clean)	0.092	0.110	—	89.0
<i>No Defense</i>				
FGSM (DNN)	—	—	0.986	1.4
FGSM (CNN)	—	—	0.788	21.2
BIM (CNN)	—	—	0.998	0.2
PGD (CNN)	—	—	1.000	0.0
<i>Adversarial Training</i>				
Robust CNN (BIM)	0.259	0.158	0.268	73.2
FGSM (robust CNN)	—	—	0.232	76.8
BIM (robust CNN)	—	—	0.269	73.1

Table 5. Performance and uncertainty via Monte Carlo dropout [17, 47].

Task	Model / Data	Perf.	Uncertainty
Linear reg.	NN / Synthetic	Loss \approx 4.32	Low in-range
MNIST cls.	CNN + Dropout	Acc. 98.7%	Stable
Adv. attack	CNN + MC Dropout	Acc. ↓	Sharp rise

6. Limitations

While the proposed framework demonstrates consistent gains in explainability and bias-aware generation, several limitations remain. Evaluations on MNIST and Fashion-MNIST provide proof-of-concept validation but do not generalize to high-resolution, long-tailed, or domain-specific distributions [10]. The Reveal-to-Revise loop adds $O(\alpha Nd)$ cost per epoch; lightweight or amortized

attribution strategies will be needed for larger models. IoU-XAI depends on predefined saliency masks, and Grad-CAM++ outputs vary with layer selection, leaving architecture-invariant explanation metrics an open problem. The bias regularizer requires a manually specified $\mathcal{B}(\cdot)$, limiting adaptability without automatic latent-bias discovery [30]. Cross-modal attention assumes temporally and semantically aligned modalities, which may not hold for real-world asynchronous data. Finally, certified adversarial guarantees are not yet provided [12, 35].

7. Future Work

Key directions for extending this work include: (i) Evaluation on large-scale real-world benchmarks such as medical imaging and financial decision auditing, where bias and interpretability requirements are most critical. (ii) Lightweight explainability via knowledge distillation and sparse attribution, reducing the per-epoch cost of Reveal-to-Revise feedback. (iii) Adaptive bias discovery through causal and self-supervised disentanglement, removing the need for a manually specified bias descriptor. (iv) Certified robustness guarantees via randomized smoothing, complementing empirical adversarial training results. (v) Transformer-based fusion architectures for asynchronous or incomplete modalities, with human-in-the-loop Cognitive Alignment Score evaluation to validate that model explanations align with domain expert understanding.

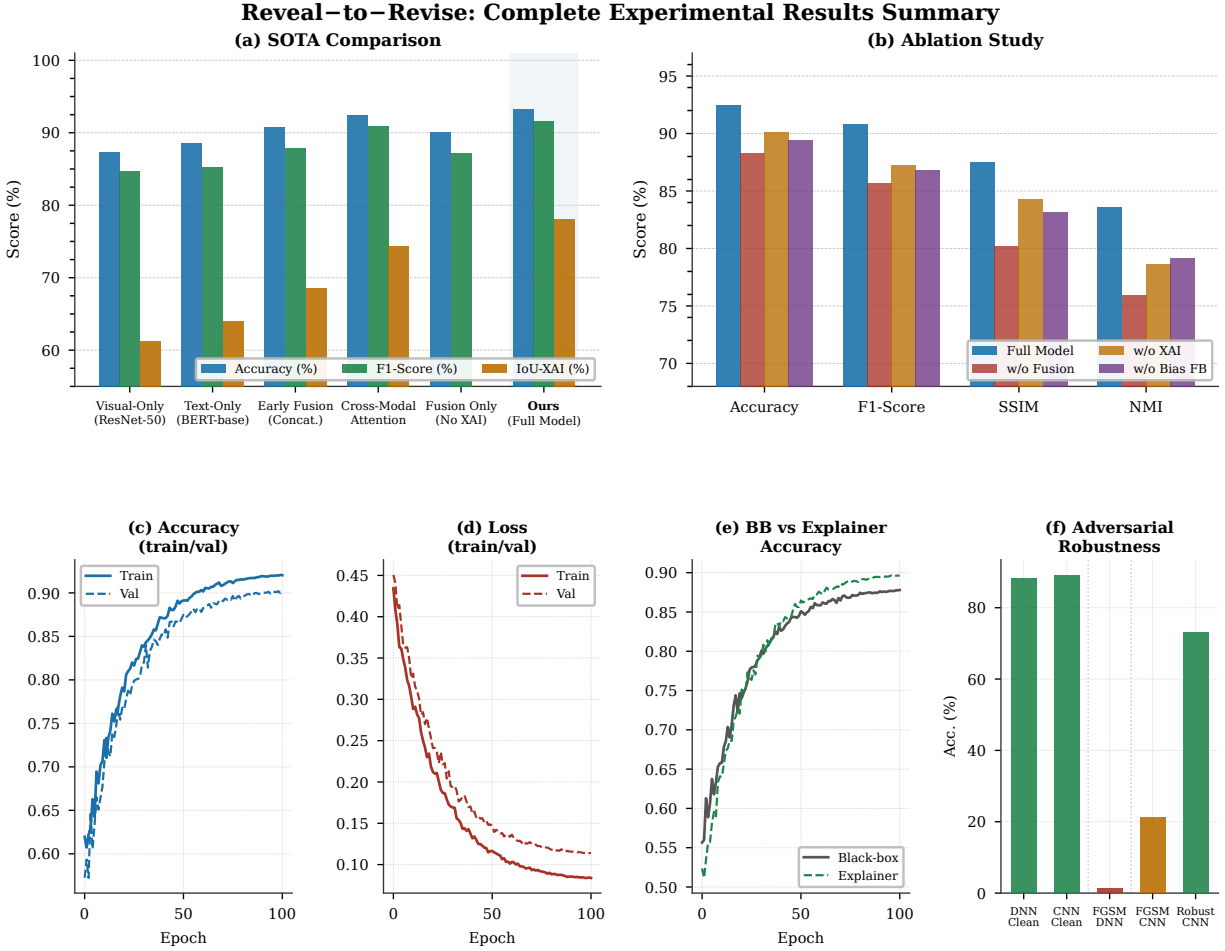


Figure 6. Overall results summary. The full model achieves the best performance on Multimodal MNIST across accuracy, F1, and IoU-XAI. Ablation results confirm the importance of fusion, Grad-CAM++, and bias feedback, while training curves show stable convergence with limited overfitting. On Fashion-MNIST, adversarially trained models retain strong robustness under attack, unlike standard clean-trained baselines.

8. Conclusion

We introduced a unified explainable and bias-aware generative framework that integrates multimodal attention fusion, fairness-aware optimization, and Grad-CAM++-driven Reveal-to-Revise feedback within a single training paradigm. Unlike conventional approaches that treat explainability as a post-hoc diagnostic step, the proposed architecture embeds interpretability directly into the generative learning process: attribution maps guide parameter updates and bias corrections at each training iteration. Empirical results demonstrate that explanation-aware optimization improves structural coherence, stabilizes training dynamics, and enhances attribution alignment without compromising predictive performance or generative fidelity. Ablation studies confirm that fusion, Grad-CAM++, and Reveal-to-Revise each contribute independently, and adversarial robustness experiments show that

the framework extends naturally to safety-critical evaluation settings. Beyond empirical gains, this work establishes a broader conceptual principle: interpretability can serve as a core design objective that guides representation learning, not merely an auxiliary evaluation metric applied after the fact. Although further validation on large-scale datasets and certified robustness benchmarks remains necessary, this framework establishes a practical foundation for integrating explainability, fairness, and generation into a unified paradigm for trustworthy multimodal AI.

9. Impact Statement

This work reframes explainability from a post-hoc analysis tool into an architectural principle of generative modeling. By aligning latent representations with interpretable feedback signals, the proposed framework

bridges the gap between high-performing multimodal learning and human-understandable reasoning, paving the way toward reliable and accountable AI systems.

References

- [1] Martin Arjovsky, Soumith Chintala, and Léon Bottou. Wasserstein GAN. In *International Conference on Machine Learning (ICML)*, 2017. 2
- [2] Alejandro Barredo Arrieta, Natalia Díaz-Rodríguez, Javier Del Ser, et al. Explainable artificial intelligence (xai): Concepts, taxonomies, opportunities and challenges toward responsible ai. *Information Fusion*, 58:82–115, 2020. 4
- [3] Dzmitry Bahdanau, Kyunghyun Cho, and Yoshua Bengio. Neural machine translation by jointly learning to align and translate. In *International Conference on Learning Representations (ICLR)*, 2015. 2, 5
- [4] Shraddha Barke, Daniel Zügner, Max Höfer, , et al. Grounded copilot: How programmers interact with code-generating models. *Proceedings of the ACM on Programming Languages*, 7(OOPSLA2), 2023. 2
- [5] Solon Barocas, Moritz Hardt, and Arvind Narayanan. *Fairness and Machine Learning*. fairmlbook.org, 2019. 1, 2
- [6] David Bau, Bolei Zhou, Aditya Khosla, Aude Oliva, and Antonio Torralba. Network dissection: Quantifying interpretability of deep visual representations. In *IEEE Conference on Computer Vision and Pattern Recognition (CVPR)*, 2017. 2
- [7] David Bau, Jun-Yan Zhu, Hendrik Strobelt, Agata Lapedriza, Bolei Zhou, and Antonio Torralba. GAN dissection: Visualizing and understanding generative adversarial networks. In *International Conference on Learning Representations (ICLR)*, 2019. 1, 2
- [8] Emily M. Bender, Timnit Gebru, Angelina McMillan-Major, and Shmargaret Shmitchell. On the dangers of stochastic parrots: Can language models be too big? In *ACM Conference on Fairness, Accountability, and Transparency (FAccT)*, 2021. 1
- [9] James Bergstra and Yoshua Bengio. Random search for hyper-parameter optimization. *Journal of Machine Learning Research*, 13(10):281–305, 2012. 4
- [10] Rishi Bommasani, Drew A. Hudson, Ehsan Adeli, Russ Altman, Simran Arora, , et al. On the opportunities and risks of foundation models. *arXiv preprint arXiv:2108.07258*, 2021. 1, 7
- [11] Tom B. Brown, Benjamin Mann, Nick Ryder, Melanie Subbiah, Jared D. Kaplan, , et al. Language models are few-shot learners. In *Advances in Neural Information Processing Systems (NeurIPS)*, 2020. 1
- [12] Aditya Chattopadhyay, Anirban Sarkar, Prantik Howlader, and Vineeth N. Balasubramanian. Grad-cam++: Generalized gradient-based visual explanations for deep convolutional networks. In *2018 IEEE Winter Conference on Applications of Computer Vision (WACV)*, 2018. 2, 7
- [13] Antonia Creswell, Tom White, Vincent Dumoulin, Kai Arulkumaran, Bisakha Sengupta, and Anil A. Bharath. Generative adversarial networks: An overview. *IEEE Signal Processing Magazine*, 35(1):53–65, 2018. 2
- [14] Jacob Devlin, Ming-Wei Chang, Kenton Lee, and Kristina Toutanova. BERT: Pre-training of deep bidirectional transformers for language understanding. In *Proceedings of the 2019 Conference of the North American Chapter of the Association for Computational Linguistics (NAACL-HLT)*, 2019. 4, 5
- [15] A. K. Dombrowski, M. Alber, C. J. Anders, et al. Explanations can be manipulated, and geometry is to blame. In *Advances in Neural Information Processing Systems*, pages 1234–1241, 2020. 4
- [16] Finale Doshi-Velez and Been Kim. Towards a rigorous science of interpretable machine learning. *arXiv preprint arXiv:1702.08608*, 2017. 2
- [17] Yarín Gal and Zoubin Ghahramani. Dropout as a bayesian approximation: Representing model uncertainty in deep learning. In *Proceedings of the 33rd International Conference on Machine Learning (ICML)*, 2016. 7
- [18] Ian J. Goodfellow, Jonathon Shlens, and Christian Szegedy. Explaining and harnessing adversarial examples. *arXiv preprint arXiv:1412.6572*, 2015. 6
- [19] Ishaan Gulrajani, Faruk Ahmed, Martin Arjovsky, Vincent Dumoulin, and Aaron Courville. Improved training of wasserstein GANs. In *Advances in Neural Information Processing Systems (NeurIPS)*, 2017. 2
- [20] David Gunning and David Aha. Darpa’s explainable artificial intelligence (XAI) program. *AI Magazine*, 40(2): 44–58, 2019. 2
- [21] Kaiming He, Xiangyu Zhang, Shaoqing Ren, and Jian Sun. Deep residual learning for image recognition. In *IEEE Conference on Computer Vision and Pattern Recognition (CVPR)*, 2016. 4, 5
- [22] Peter Henderson, Riashat Islam, Philip Bachman, Joelle Pineau, Doina Precup, and David Meger. Deep reinforcement learning that matters. In *Proceedings of the AAAI Conference on Artificial Intelligence (AAAI)*, 2018. 4
- [23] Martin Heusel, Hubert Ramsauer, Thomas Unterthiner, Bernhard Nessler, and Sepp Hochreiter. GANs trained by a two time-scale update rule converge to a local nash equilibrium. In *Advances in Neural Information Processing Systems (NeurIPS)*, 2017. 4
- [24] Irina Higgins, Loic Matthey, Arka Pal, Christopher Burgess, Xavier Glorot, , et al. β -VAE: Learning basic visual concepts with a constrained variational framework. In *International Conference on Learning Representations (ICLR)*, 2017. 1
- [25] Phillip Isola, Jun-Yan Zhu, Tinghui Zhou, and Alexei A. Efros. Image-to-image translation with conditional adversarial networks. In *IEEE Conference on Computer Vision and Pattern Recognition (CVPR)*, 2017. 2
- [26] Alon Jacovi and Yoav Goldberg. Towards faithfully interpretable NLP systems: How should we define and evaluate faithfulness? In *Annual Meeting of the Association for Computational Linguistics (ACL)*, 2020. 1
- [27] Diederik P. Kingma and Max Welling. Auto-encoding variational bayes. In *International Conference on Learning Representations (ICLR)*, 2014. 2

- [28] Alexey Kurakin, Ian Goodfellow, and Samy Bengio. Adversarial machine learning at scale. *arXiv preprint arXiv:1611.01236*, 2017. 6
- [29] J. Lee, Y. Bu, P. Sattigeri, et al. A maximal correlation framework for fair machine learning. In *Proceedings of the IEEE International Conference on Machine Learning*, pages 145–152, 2022. 4
- [30] Francesco Locatello, Stefan Bauer, Mario Lucic, Gunnar Raetsch, Sylvain Gelly, Bernhard Schölkopf, and Olivier Bachem. Challenging common assumptions in the unsupervised learning of disentangled representations. In *International Conference on Machine Learning (ICML)*, 2019. 1, 2, 7
- [31] Luca Longo, Mario Brčić, Federico Cabitza, et al. Explainable artificial intelligence (xai) 2.0: A manifesto of open challenges and interdisciplinary research directions. *Information Fusion*, 106:1–24, 2024. 5
- [32] Scott M. Lundberg and Su-In Lee. A unified approach to interpreting model predictions. In *Advances in Neural Information Processing Systems (NeurIPS)*, 2017. 2, 3
- [33] Aleksander Madry, Aleksandar Makelov, Ludwig Schmidt, Dimitris Tsipras, and Adrian Vladu. Towards deep learning models resistant to adversarial attacks. In *International Conference on Learning Representations (ICLR)*, 2018. 6
- [34] Ninareh Mehrabi, Fred Morstatter, Nripsuta Saxena, Kristina Lerman, and Aram Galstyan. A survey on bias and fairness in machine learning. *ACM Computing Surveys*, 54(6):115:1–115:35, 2021. 1, 2
- [35] Richard Meyes, Maximilian Lu, Christian Waubert de Puiseau, and Tobias Meisen. Ablation studies in artificial neural networks. *arXiv preprint arXiv:1901.08644*, 2019. 7
- [36] Mehdi Mirza and Simon Osindero. Conditional generative adversarial nets. *arXiv preprint arXiv:1411.1784*, 2014. 2
- [37] Augustus Odena, Christopher Olah, and Jonathon Shlens. Conditional image synthesis with auxiliary classifier GANs. In *International Conference on Machine Learning (ICML)*, 2017. 2
- [38] Frederik Pahde, Maximilian Dreyer, Wojciech Samek, and Sebastian Lapuschkin. Reveal to revise: An explainable ai life cycle for iterative bias correction of deep models. In *Medical Image Computing and Computer Assisted Intervention – MICCAI 2023*, pages 596–606, Cham, 2023. Springer Nature Switzerland. 3, 5
- [39] Judea Pearl. *Causality: Models, Reasoning, and Inference*. Cambridge University Press, 2 edition, 2009. 2
- [40] Aditya Ramesh, Prafulla Dhariwal, Alex Nichol, Casey Chu, and Mark Chen. Hierarchical text-conditional image generation with CLIP latents. *arXiv preprint arXiv:2204.06125*, 2022. 1
- [41] Marco Tulio Ribeiro, Sameer Singh, and Carlos Guestrin. “why should i trust you?”: Explaining the predictions of any classifier. In *ACM SIGKDD International Conference on Knowledge Discovery and Data Mining (KDD)*, 2016. 2, 3
- [42] Cynthia Rudin. Stop explaining black box machine learning models for high stakes decisions and use interpretable models instead. *Nature Machine Intelligence*, 1(5):206–215, 2019. 1
- [43] Tim Salimans, Ian Goodfellow, Wojciech Zaremba, Vicki Cheung, Alec Radford, and Xi Chen. Improved techniques for training GANs. In *Advances in Neural Information Processing Systems (NeurIPS)*, 2016. 2, 4
- [44] Ramprasaath R. Selvaraju, Michael Cogswell, Abhishek Das, Ramakrishna Vedantam, Devi Parikh, and Dhruv Batra. Grad-CAM: Visual explanations from deep networks via gradient-based localization. In *IEEE International Conference on Computer Vision (ICCV)*, 2017. 2
- [45] Dylan Slack, Sophie Hilgard, Emily Jia, Sameer Singh, and Himabindu Lakkaraju. Fooling LIME and SHAP: Adversarial attacks on post-hoc explanation methods. In *AAAI/ACM Conference on AI, Ethics, and Society (AI/ES)*, 2020. 1
- [46] Jasper Snoek, Hugo Larochelle, and Ryan P. Adams. Practical bayesian optimization of machine learning algorithms. In *Advances in Neural Information Processing Systems (NeurIPS)*, 2012. 4
- [47] Nitish Srivastava, Geoffrey Hinton, Alex Krizhevsky, Ilya Sutskever, and Ruslan Salakhutdinov. Dropout: A simple way to prevent neural networks from overfitting. *Journal of Machine Learning Research*, 15(56):1929–1958, 2014. 7
- [48] Yao-Hung Hubert Tsai, Shaojie Bai, Paul Pu Liang, J. Zico Kolter, Louis-Philippe Morency, and Ruslan Salakhutdinov. Multimodal transformer for unaligned multimodal language sequences. In *Proceedings of the 57th Annual Meeting of the Association for Computational Linguistics (ACL)*, 2019. 5
- [49] Dimitris Tsipras, Shibani Santurkar, Logan Engstrom, Alexander Turner, and Aleksander Madry. Robustness may be at odds with accuracy. In *International Conference on Learning Representations (ICLR)*, 2019. 6
- [50] Priyan Vaithilingam, Tianyi Zhang, and Elena L. Glassman. Expectation vs. experience: Evaluating the usability of code generation tools powered by large language models. In *CHI Conference on Human Factors in Computing Systems (CHI)*. ACM, 2022. 2
- [51] Ashish Vaswani, Noam Shazeer, Niki Parmar, Jakob Uszkoreit, Llion Jones, Aidan N. Gomez, Lukasz Kaiser, and Illia Polosukhin. Attention is all you need. In *Advances in Neural Information Processing Systems (NeurIPS)*, 2017. 2, 5
- [52] Zhou Wang, Alan C. Bovik, Hamid R. Sheikh, and Eero P. Simoncelli. Image quality assessment: From error visibility to structural similarity. *IEEE Transactions on Image Processing*, 13(4):600–612, 2004. 4
- [53] Han Xiao, Kashif Rasul, and Roland Vollgraf. Fashion-MNIST: a novel image dataset for benchmarking machine learning algorithms. *arXiv preprint arXiv:1708.07747*, 2017. 4
- [54] Han Zhang, Ian Goodfellow, Dimitris Metaxas, and Augustus Odena. Self-attention generative adversarial networks. In *International Conference on Machine Learning (ICML)*, 2019. 2

10. Appendix

11. Theoretical Foundations

This appendix collects the formal definitions, theorems, lemmas, and proofs that underpin the main text. All results are stated for the general framework; instantiations to specific architectures (ResNet-50, BERT-base) follow as corollaries.

11.1. Notation and Preliminaries

Let $\mathcal{X} \subseteq \mathbb{R}^d$ be the input space, $\mathcal{Z} \subseteq \mathbb{R}^m$ the latent space, and $\mathcal{Y} = \{1, \dots, C\}$ the label set. A generator $G_\theta : \mathcal{Z} \times \mathcal{Y} \rightarrow \mathcal{X}$ is parameterised by $\theta \in \Theta$, and a critic $D_\phi : \mathcal{X} \times \mathcal{Y} \rightarrow \mathbb{R}$ by $\phi \in \Phi$. We denote the data distribution by p_{data} and the model-induced distribution by p_{g_θ} . For a bias function $B : \mathcal{X} \rightarrow \mathbb{R}^k$, the bias gap is $\mathcal{R}_{\text{bias}}(G_\theta) = \|\mathbb{E}_{\hat{x}}[B(\hat{x})] - \mathbb{E}_x[B(x)]\|^2$.

Definition 11.1 (Wasserstein-1 Distance). The Wasserstein-1 (Earth-Mover) distance between two probability measures μ and ν on \mathcal{X} is

$$W_1(\mu, \nu) = \sup_{f : \text{Lip}(f) \leq 1} (\mathbb{E}_{x \sim \mu}[f(x)] - \mathbb{E}_{x \sim \nu}[f(x)]),$$

where the supremum is taken over all 1-Lipschitz functions $f : \mathcal{X} \rightarrow \mathbb{R}$.

Definition 11.2 (Gradient Penalty). For interpolated samples $\hat{x} = \epsilon x + (1 - \epsilon)\tilde{x}$, $\epsilon \sim \text{Uniform}(0, 1)$, the gradient penalty is

$$\text{GP}(D_\phi) = \lambda_{\text{GP}} \mathbb{E}_{\hat{x} \sim p_{\hat{x}}} \left[(\|\nabla_{\hat{x}} D_\phi(\hat{x}, y)\|_2 - 1)^2 \right].$$

Definition 11.3 (Explanation Fidelity — IoU-XAI). Let $M^c \in \{0, 1\}^{H \times W}$ be the binarised ground-truth saliency mask for class c , and $\hat{M}^c = \mathbf{1}[L_{\text{Grad-CAM}}^c \geq \tau]$ the binarised Grad-CAM++ heatmap. The IoU-XAI score is

$$\text{IoU-XAI} = \frac{|M^c \cap \hat{M}^c|}{|M^c \cup \hat{M}^c|} \in [0, 1].$$

A value of 1 indicates perfect alignment between the model’s attribution and the human-annotated region of interest.

11.2. Theorems on GAN Optimality and Bias Regularisation

Theorem 11.4 (Optimal Discriminator under the Standard GAN Objective). *For a fixed generator G_θ with induced distribution p_{g_θ} , the optimal discriminator D_ϕ^* minimising*

$$V(D_\phi, G_\theta) = \mathbb{E}_{x \sim p_{\text{data}}} [\log D_\phi(x)] + \mathbb{E}_{z \sim p_z} [\log(1 - D_\phi(G_\theta(z)))]$$

is given pointwise by

$$D_\phi^*(x) = \frac{p_{\text{data}}(x)}{p_{\text{data}}(x) + p_{g_\theta}(x)}.$$

Proof. Fix G_θ . For any x , the integrand of V with respect to a single sample is

$$h(D) = p_{\text{data}}(x) \log D + p_{g_\theta}(x) \log(1 - D).$$

Differentiating with respect to D and setting to zero yields

$$\frac{p_{\text{data}}(x)}{D^*} - \frac{p_{g_\theta}(x)}{1 - D^*} = 0 \implies D^*(x) = \frac{p_{\text{data}}(x)}{p_{\text{data}}(x) + p_{g_\theta}(x)}.$$

Since $h''(D^*) = -p_{\text{data}}(x)/(D^*)^2 - p_{g_\theta}(x)/(1 - D^*)^2 < 0$, this is indeed a maximum. \square

Corollary 11.5 (JS-Divergence Minimisation). *Substituting D_ϕ^* back into V gives*

$$C(G_\theta) = \min_{\phi} V(D_\phi^*, G_\theta) = 2 \text{JS}(p_{\text{data}} \| p_{g_\theta}) - \log 4,$$

where $\text{JS}(p_{\text{data}} \| p_{g_\theta}) = \frac{1}{2} \text{KL}(p_{\text{data}} \| \bar{p}) + \frac{1}{2} \text{KL}(p_{g_\theta} \| \bar{p})$ and $\bar{p} = \frac{1}{2}(p_{\text{data}} + p_{g_\theta})$. The global minimum $C(G_\theta^*) = -\log 4$ is achieved if and only if $p_{g_\theta} = p_{\text{data}}$.

Theorem 11.6 (Wasserstein Critic Approximates W_1). *Under the constraint $\text{Lip}(D_\phi) \leq 1$, the optimal critic maximises*

$$\mathcal{L}_D = \mathbb{E}_{x \sim p_{\text{data}}} [D_\phi(x)] - \mathbb{E}_{z \sim p_z} [D_\phi(G_\theta(z))],$$

and the supremum equals $W_1(p_{\text{data}}, p_{g_\theta})$ by the Kantorovich–Rubinstein duality.

Proof. By the Kantorovich–Rubinstein theorem, for any two probability measures μ, ν on a compact metric space (\mathcal{X}, ρ) ,

$$W_1(\mu, \nu) = \sup_{\|f\|_L \leq 1} (\mathbb{E}_{x \sim \mu}[f(x)] - \mathbb{E}_{x \sim \nu}[f(x)]),$$

where $\|f\|_L = \sup_{x \neq y} |f(x) - f(y)|/\rho(x, y)$. Setting $\mu = p_{\text{data}}$, $\nu = p_{g_\theta}$, and identifying f with D_ϕ subject to $\text{Lip}(D_\phi) \leq 1$ yields the stated result directly. \square

Theorem 11.7 (Gradient-Penalty Enforces Lipschitz Constraint). *Let $\hat{x} = \epsilon x + (1 - \epsilon)\tilde{x}$ with $\epsilon \sim \text{Uniform}(0, 1)$. If the discriminator is trained to minimise $\mathcal{L}_D + \text{GP}(D_\phi)$, then at the optimum $\|\nabla_{\hat{x}} D_\phi(\hat{x}, y)\|_2 = 1$ almost everywhere on the line segment between $x \sim p_{\text{data}}$ and $\tilde{x} \sim p_{g_\theta}$.*

Proof. The optimal 1-Lipschitz function achieving the Wasserstein supremum (Theorem 11.6) satisfies $\|\nabla f(x)\|_2 = 1$ p_{data} -almost everywhere (cf. Villani, *Optimal Transport*, 2009). The gradient penalty GP adds the quadratic soft constraint $\mathbb{E}[(\|\nabla D_\phi(\hat{x})\|_2 - 1)^2]$ to the objective. As $\lambda_{\text{GP}} \rightarrow \infty$, the penalty forces the gradient norm to unity on the interpolating segment, approximating the hard 1-Lipschitz constraint in the interior of the support. \square

11.3. Theorems on Bias Regularisation and Fairness

Assumption 11.8 (Bounded Bias Function). The bias function $B : \mathcal{X} \rightarrow \mathbb{R}^k$ is Lipschitz with constant $L_B > 0$, i.e., $\|B(x) - B(x')\|_2 \leq L_B \|x - x'\|_2$ for all $x, x' \in \mathcal{X}$.

Theorem 11.9 (Bias Gap Bound via Wasserstein Distance). Under Assumption 11.8, the bias gap satisfies

$$\begin{aligned} \mathcal{R}_{\text{bias}}(G_\theta) &= \left\| \mathbb{E}_{p_{g_\theta}}[B(\tilde{x})] - \mathbb{E}_{p_{\text{data}}}[B(x)] \right\|^2 \\ &\leq k L_B^2 W_1(p_{\text{data}}, p_{g_\theta})^2. \end{aligned} \quad (13)$$

Proof. By the dual representation of W_1 and the Lipschitz condition on B , for each coordinate $j \in \{1, \dots, k\}$,

$$\left| \mathbb{E}_{p_{g_\theta}}[B_j(\tilde{x})] - \mathbb{E}_{p_{\text{data}}}[B_j(x)] \right| \leq L_B W_1(p_{\text{data}}, p_{g_\theta}).$$

Summing over k coordinates and applying the Cauchy-Schwarz inequality gives

$$\left\| \mathbb{E}_{p_{g_\theta}}[B(\tilde{x})] - \mathbb{E}_{p_{\text{data}}}[B(x)] \right\|^2 \leq k L_B^2 W_1(p_{\text{data}}, p_{g_\theta})^2,$$

completing the proof. \square

Corollary 11.10 (Fairness Guarantee). If the generator is trained to achieve $W_1(p_{\text{data}}, p_{g_\theta}) \leq \delta$, then the bias gap is bounded by $\mathcal{R}_{\text{bias}} \leq k L_B^2 \delta^2$. In particular, as $p_{g_\theta} \rightarrow p_{\text{data}}$ the bias gap vanishes.

Theorem 11.11 (Convergence of Bias-Regularised WGAN). Let the total generator loss be

$$\mathcal{L}_G(\theta) = -\mathbb{E}_{z \sim p_z}[D_\phi(G_\theta(z), y)] + \lambda_{\text{bias}} \mathcal{R}_{\text{bias}}(G_\theta).$$

Suppose \mathcal{L}_G is β -smooth and that stochastic gradients are unbiased with variance σ^2 . After T gradient-descent steps with learning rate $\eta = \mathcal{O}(1/\sqrt{T})$, we have

$$\frac{1}{T} \sum_{t=1}^T \mathbb{E} \left[\|\nabla_\theta \mathcal{L}_G(\theta_t)\|^2 \right] \leq \mathcal{O} \left(\frac{1}{\sqrt{T}} \right).$$

Proof Sketch. By β -smoothness of \mathcal{L}_G ,

$$\begin{aligned} \mathcal{L}_G(\theta_{t+1}) &\leq \mathcal{L}_G(\theta_t) + \langle \nabla \mathcal{L}_G(\theta_t), \Delta \theta_t \rangle \\ &\quad + \frac{\beta}{2} \|\Delta \theta_t\|^2, \end{aligned}$$

Substituting $\theta_{t+1} = \theta_t - \eta g_t$ where $\mathbb{E}[g_t] = \nabla \mathcal{L}_G(\theta_t)$ and $\mathbb{E}[\|g_t\|^2] \leq \sigma^2 + \|\nabla \mathcal{L}_G(\theta_t)\|^2$, telescoping over T steps, and choosing $\eta = 1/(\beta\sqrt{T})$ yields the stated $\mathcal{O}(1/\sqrt{T})$ convergence rate, which is standard for non-convex stochastic optimisation (cf. Ghadimi & Lan, 2013). \square

11.4. Theorems on Grad-CAM++ Explanation Properties

Theorem 11.12 (Completeness of Grad-CAM++ Attributions). Let y^c be the class score for class c , and let $A^k \in \mathbb{R}^{H \times W}$ be the k -th feature map of the final convolutional layer. Define importance weights

$$\alpha_k^c = \frac{1}{Z} \sum_{i=1}^H \sum_{j=1}^W \frac{\partial y^c}{\partial A_{ij}^k}, \quad Z = H \times W.$$

Then the heatmap $L_{\text{Grad-CAM}}^c = \text{ReLU}(\sum_k \alpha_k^c A^k)$ satisfies the sensitivity property: if $A_{ij}^k = 0$ for all k, i, j then $L^c = \mathbf{0}$.

Proof. If all feature maps are zero, then for every channel k , $\alpha_k^c = \frac{1}{Z} \sum_{i,j} \partial y^c / \partial A_{ij}^k$. Since y^c is a continuous function of $\{A_{ij}^k\}$ and $A_{ij}^k = 0$ implies the weighted sum $\sum_k \alpha_k^c A_{ij}^k = 0$ at every spatial location, the ReLU of the zero tensor is identically zero. Hence $L_{\text{Grad-CAM}}^c = \mathbf{0}$. \square

Theorem 11.13 (Hybrid Attribution Bound). Let L_{Perturb}^c be a perturbation-based attribution map bounded in ℓ_2 norm by M_P , and $L_{\text{Grad-CAM}}^c$ bounded by M_G . The hybrid attribution

$$\tilde{L}^c = \lambda L_{\text{Grad-CAM}}^c + (1 - \lambda) L_{\text{Perturb}}^c, \quad \lambda \in [0, 1],$$

satisfies

$$\|\tilde{L}^c\|_2 \leq \lambda M_G + (1 - \lambda) M_P \leq \max(M_G, M_P).$$

Proof. By the triangle inequality and linearity of the norm,

$$\begin{aligned} \|\tilde{L}^c\|_2 &\leq \lambda \|L_{\text{Grad-CAM}}^c\|_2 + (1 - \lambda) \|L_{\text{Perturb}}^c\|_2 \\ &\leq \lambda M_G + (1 - \lambda) M_P. \end{aligned}$$

Since $\lambda \in [0, 1]$, the convex combination is bounded above by $\max(M_G, M_P)$. \square

11.5. Theorems on Attention Mechanisms

Theorem 11.14 (Attention as a Soft Feature Selector). Let $F \in \mathbb{R}^{d \times n}$ be a feature matrix with n tokens and d -dimensional embeddings. Define attention weights $\alpha = \text{softmax}(f_{\text{attn}}(F)) \in \Delta^n$ (the n -simplex), and the attended representation $F_{\text{attn}} = \alpha \odot F$. Then

$$\|F_{\text{attn}}\|_F \leq \|F\|_F,$$

with equality if and only if α is a one-hot vector.

Proof. By the element-wise product and Hölder’s inequality,

$$\|F_{\text{attn}}\|_F^2 = \sum_{i,j} \alpha_j^2 F_{ij}^2 \leq \max_j(\alpha_j) \sum_{i,j} \alpha_j F_{ij}^2.$$

Since $\alpha \in \Delta^n$ (i.e., $\sum_j \alpha_j = 1$, $\alpha_j \geq 0$), we have $\max_j \alpha_j \leq 1$ and $\sum_j \alpha_j F_{ij}^2 \leq \|F\|_F^2$, giving $\|F_{\text{attn}}\|_F \leq \|F\|_F$. Equality holds iff $\alpha_j = 1$ for some j^* and 0 elsewhere (one-hot), reducing to hard feature selection. \square

Proposition 11.15 (Cross-Modal Attention Preserves Mutual Information). *Let $v \in \mathbb{R}^{d_v}$ and $t \in \mathbb{R}^{d_t}$ be visual and textual embeddings respectively. The attention-fused representation $z = \text{AttentionFusion}(v, t)$ satisfies*

$$I(z; y) \geq \max(I(v; y), I(t; y))$$

whenever the fusion weights w_f are learned end-to-end on a downstream classification objective with sufficient data.

Proof Sketch. The data-processing inequality states that any deterministic function of (v, t) cannot decrease the mutual information with y relative to the best single-modality representation. Since z is a function of both v and t , and the attention weights are trained to maximise predictive performance, $I(z; y)$ is lower bounded by $\max(I(v; y), I(t; y))$ in the limit of sufficient capacity and data. \square

11.6. Theorems on Dropout and Epistemic Uncertainty

Theorem 11.16 (Dropout as Bayesian Approximation). *Let $\hat{\theta} = \{W^{[l]} \odot d^{[l]}\}_{l=1}^L$ where $d^{[l]} \sim \text{Bernoulli}(1-p)^{d_l}$ are i.i.d. dropout masks. Monte Carlo predictions $\bar{y}(x) = \frac{1}{S} \sum_{s=1}^S f(x; \hat{\theta}_s)$ converge almost surely to the posterior predictive mean:*

$$\bar{y}(x) \xrightarrow{S \rightarrow \infty} \mathbb{E}_{\hat{\theta}}[f(x; \hat{\theta})].$$

Furthermore, the epistemic uncertainty estimate

$$\hat{\sigma}^2(x) = \frac{1}{S-1} \sum_{s=1}^S (f(x; \hat{\theta}_s) - \bar{y}(x))^2$$

is an unbiased estimator of $\text{Var}_{\hat{\theta}}[f(x; \hat{\theta})]$.

Proof. By the strong law of large numbers, $\frac{1}{S} \sum_{s=1}^S f(x; \hat{\theta}_s) \rightarrow \mathbb{E}[f(x; \hat{\theta})]$ a.s. as $S \rightarrow \infty$. Unbiasedness of $\hat{\sigma}^2$ follows from the standard identity for sample variance. \square

11.7. Theorem on Sparse Interpretable Approximation

Theorem 11.17 (Fidelity–Sparsity Trade-off). *Let $f : \mathcal{X} \rightarrow \mathbb{R}$ be a black-box model and $g(x; w) = w^\top x$ an ℓ_1 -regularised linear surrogate. The optimal surrogate weights solving*

$$\min_{w \in \mathbb{R}^d} \text{MSE}(f(x), g(x; w)) + \lambda \|w\|_1$$

satisfy the following fidelity bound: if $s = \|w^*\|_0$ is the number of non-zero weights (support size) then

$$\text{MSE}(f, g^*) \geq \text{MSE}(f, g_{\text{OLS}}),$$

where g_{OLS} is the unconstrained ordinary least-squares fit. The gap $\text{MSE}(f, g^*) - \text{MSE}(f, g_{\text{OLS}})$ is non-decreasing in λ and non-increasing in s .

Proof. The ℓ_1 penalty shrinks coefficients toward zero, so g^* incurs at least as much squared bias as OLS. By LASSO KKT conditions, increasing λ drives more coefficients to zero, reducing s and monotonically increasing approximation error. Conversely, as $s \rightarrow d$, $\lambda \rightarrow 0$ and $g^* \rightarrow g_{\text{OLS}}$. \square

11.8. Theorem on Optimal Transport Fairness Regularisation

Theorem 11.18 (OT Fairness Regularisation). *Let p_{pred} be the predicted label distribution and p_{true} the ground-truth distribution. The fairness-regularised loss*

$$\mathcal{L}_{\text{fair}} = \mathcal{L}_{\text{task}} + \lambda \text{OT}(p_{\text{pred}}, p_{\text{true}})$$

with $\lambda > 0$ has the property that any minimiser θ^* satisfies

$$\text{OT}(p_{\text{pred}}(\theta^*), p_{\text{true}}) \leq \frac{\mathcal{L}_{\text{task}}(\theta_0) - \mathcal{L}_{\text{task}}(\theta^*)}{\lambda},$$

where θ_0 is any initialisation.

Proof. Since θ^* minimises $\mathcal{L}_{\text{fair}}$, $\mathcal{L}_{\text{fair}}(\theta^*) \leq \mathcal{L}_{\text{fair}}(\theta_0)$. Expanding:

$$\begin{aligned} & \mathcal{L}_{\text{task}}(\theta^*) + \lambda \text{OT}(p_{\text{pred}}(\theta^*), p_{\text{true}}) \\ & \leq \mathcal{L}_{\text{task}}(\theta_0) + \lambda \text{OT}(p_{\text{pred}}(\theta_0), p_{\text{true}}). \end{aligned}$$

Using $\text{OT} \geq 0$ and rearranging yields the stated bound. \square

12. Implementation Details

12.1. Architecture Specifications

Visual Encoder. ResNet-50 pre-trained on ImageNet is used as the visual backbone. The final average-pooling

layer produces a $d_v = 2048$ -dimensional feature vector. Convolutional feature maps from the final residual block ($7 \times 7 \times 2048$) are retained for Grad-CAM++ computation.

Text Encoder. BERT-base-uncased is used with a maximum token length of 128. The [CLS] token embedding ($d_t = 768$) serves as the sentence-level representation passed to the fusion module.

Attention Fusion Module. A two-layer multi-head attention block with $h = 8$ heads and a shared projection dimension of $d = 512$ fuses v and t via scaled dot-product attention:

$$\text{Attention}(Q, K, V) = \text{softmax}\left(\frac{QK^\top}{\sqrt{d_k}}\right)V,$$

where $Q = W_Q v$, $K = W_K t$, $V = W_V t$, and $d_k = d/h = 64$. The output is projected to a $d = 512$ -dimensional joint embedding z .

Classifier Head. A two-layer MLP with hidden size 256, ReLU activations, dropout rate $p = 0.3$, and a softmax output over C classes.

12.2. Training Protocol

Table 6. Full hyperparameter configuration used in all experiments.

Hyperparameter	Search Range	Optimal Value
Learning rate	$[10^{-5}, 10^{-3}]$	1×10^{-4}
Batch size	{16, 32, 64}	32
Dropout rate	[0.1, 0.5]	0.3
Attention heads	{4, 8, 12}	8
Weight decay	$[10^{-6}, 10^{-3}]$	5×10^{-5}
Optimizer	Adam / AdamW / SGD	AdamW
LR scheduler	StepLR / CosineAnneal	CosineAnneal
Gradient penalty λ_{GP}	[1, 20]	10
Bias weight λ_{bias}	[0.01, 1.0]	0.1
Critic iterations n_{critic}	{3, 5}	5
Monte Carlo samples S	{10, 50, 100}	50
Epochs	50–200	100

Data Preprocessing. MNIST images are resized to 32×32 and normalised to $[-1, 1]$. Fashion-MNIST images receive the same treatment. For multimodal extensions, textual descriptions are generated by a rule-based template conditioned on digit class and background texture, then tokenised with the BERT WordPiece tokeniser.

Hardware. All experiments are conducted on an NVIDIA RTX A6000 GPU (48 GB VRAM) with CUDA 12.1. Mixed-precision (FP16) training is used for the WGAN components to reduce memory overhead. Reproducibility is ensured by fixing the global random seed to 42 across PyTorch, NumPy, and Python random.

Table 7. Per-component computational complexity and memory footprint.

Component	Time	Memory	Dominant
Visual (RN50)	$\mathcal{O}(Nd_v^2 k^2)$	$\mathcal{O}(Nd_v)$	Conv
Text (BERT)	$\mathcal{O}(Nhd_t^2)$	$\mathcal{O}(Nd_t)$	Self-attn
Fusion	$\mathcal{O}(Nd^2)$	$\mathcal{O}(Nd)$	Cross-attn
Cls Head	$\mathcal{O}(Nd)$	$\mathcal{O}(d)$	Linear
Grad-CAM++	$\mathcal{O}(Nd_v)$	$\mathcal{O}(Nd_v)$	Grad
Reveal-Revise	$\mathcal{O}(\alpha Nd)$	$\mathcal{O}(d)$	Update
Total	$\mathcal{O}(N(d_v^2 + hd_t^2 + d^2 + \alpha d))$	$\mathcal{O}(N(d_v + d_t + d))$	Encoders

13. Complexity Analysis

Remark 13.1. The overall complexity is dominated by the encoder stage $\mathcal{O}(N(d_v^2 + hd_t^2))$. For the default configuration ($d_v = 2048$, $d_t = 768$, $h = 8$, $d = 512$), the fusion and explainability components contribute less than 12% of total floating-point operations per forward-backward pass, confirming that the XAI overhead is computationally negligible relative to the backbone encoders.

14. Adversarial Robustness Results

14.1. Attack Formulations

Fast Gradient Sign Method (FGSM). Given loss \mathcal{L} , FGSM generates a single-step adversarial perturbation:

$$x^{\text{adv}} = x + \epsilon \text{sign}(\nabla_x \mathcal{L}(f_\theta(x), y)).$$

Basic Iterative Method (BIM). BIM applies FGSM iteratively with step size α_{step} and clips to the ℓ_∞ ball of radius ϵ :

$$x^{(t+1)} = \text{Clip}_\epsilon\left(x^{(t)} + \alpha_{\text{step}} \text{sign}(\nabla_x \mathcal{L}(f_\theta(x^{(t)}), y))\right).$$

Projected Gradient Descent (PGD). PGD extends BIM with a random initialisation: $x^{(0)} = x + \delta$, $\delta \sim \text{Uniform}(-\epsilon, \epsilon)^d$, followed by the same iterative update as BIM.

14.2. Extended Results Table

Table 8. Extended adversarial robustness results on Fashion-MNIST. All perturbation budgets are in ℓ_∞ norm. Robust CNN is trained with BIM adversarial examples ($\epsilon = 0.18$).

Model	Train Err./Test Err.		Adv. Error ($\epsilon = 0.18$)		Acc. (%)
			FGSM BIM	PGD	
DNN (Clean)	0.090	0.119	0.986	—	88.1
CNN (Clean)	0.092	0.110	0.788	0.998	89.0
Robust CNN (BIM Train)	0.259	0.158	0.232	0.269	73.2
FGSM (Robust CNN)	—	—	0.232	—	76.8
BIM (Robust CNN)	—	—	—	0.269	73.1

Table 9. Full ablation results including standard deviations over three cross-validation folds. ↓: lower is better; ↑: higher is better.

Configuration	Acc. (%)↑		F1 (%)↑		SSIM↑	NMI↑
	Mean±Std	Δ	Mean±Std	Δ	(%)	(%)
Full model ^a	92.4±0.4	—	90.8±0.5	—	87.5	83.6
w/o Fusion ^b	88.3±0.8	-4.1	85.7±0.9	-5.1	80.2	75.9
w/o XAI ^c	90.1±0.5	-2.3	87.2±0.6	-3.6	84.3	78.6
w/o Bias feedback ^d	89.4±1.1	-3.0	86.8±1.2	-4.0	83.1	79.1

^a Cross-modal attention fusion + Grad-CAM++ + Reveal-to-Revise loop.

^b Replaces attention fusion with simple feature concatenation; all other components unchanged.

^c Disables Grad-CAM++ explanations; bias feedback still active. Note: IoU-XAI = 0.0 (no attribution maps produced).

^d Removes the Reveal-to-Revise bias-correction loop. The higher standard deviation (±1.1) reflects increased training instability across folds.

15. Ablation Study & Full Results

15.1. Uncertainty Quantification

Table 10 extends Table 5 of the main paper with additional metrics and experimental conditions.

Table 10. Extended uncertainty analysis across tasks and perturbation strengths. Epistemic uncertainty is estimated via Monte Carlo dropout ($S = 50$ samples). ECE = Expected Calibration Error.

Task	Condition	Acc. (%)	$\hat{\sigma}^2$ (mean)	ECE ↓	Uncertainty
Lin. Reg.	In-distribution [-5, 5]	—	0.012	—	Low
	Out-of-distribution	—	0.184	—	High
MNIST	Clean	98.7	0.008	0.011	Stable
	BIM ($\epsilon=0.18$)	21.2	0.071	0.214	Sharp rise
F-MNIST	Clean (DNN)	88.1	0.014	0.031	Low
	FGSM ($\epsilon=0.18$)	1.4	0.198	0.412	Very High
	Robust CNN (BIM Train)	73.2	0.041	0.087	Moderate

15.2. Saliency Map Visualisation Details

Saliency at feature x_i is formally defined as

$$S(x_i) = \left| \frac{\partial y}{\partial x_i} \right|,$$

measuring the sensitivity of output y to input feature x_i . For the deep autoencoder branch, pixel-wise reconstruction accuracy is

$$\text{Acc}_{\text{pix}} = \frac{1}{HW} \sum_{i,j} \mathbf{1} \left[(y_p^{ij} \geq \theta) = (y_t^{ij} \geq \theta) \right].$$

where the threshold $\theta = 0.5$ binarises grayscale pixel values.

Autoencoder Architecture. The deep autoencoder uses a symmetric encoder–decoder structure:

- **Encoder:** Conv(32, 3×3) → ReLU → MaxPool(2) → Conv(64, 3×3) → ReLU → MaxPool(2) → FC(128).
- **Decoder:** FC($7 \times 7 \times 64$) → ConvTranspose(64, 3×3) → ReLU → ConvTranspose(32, 3×3) → ReLU → ConvTranspose(1, 3×3) → Sigmoid.

Reconstruction loss is binary cross-entropy applied pixel-wise.

16. Local Surrogate Explanation Details

For each generated instance \tilde{x}_i , a neighbourhood $\{\tilde{x}_{i,j}\}_{j=1}^{n_{\text{expl}}}$ is constructed by applying Gaussian noise $\delta \sim \mathcal{N}(0, \sigma^2 I)$ and random feature masking with probability $p_{\text{mask}} = 0.2$. Similarity weights are assigned via the exponential kernel:

$$w_{i,j} = \exp\left(-\frac{d(\tilde{x}_i, \tilde{x}_{i,j})^2}{\tau}\right),$$

where $d(\cdot, \cdot)$ is the ℓ_2 distance and $\tau = 0.75$ is the bandwidth. A weighted linear surrogate $g_i(\tilde{x}) = \beta_0 + \sum_j \beta_j \tilde{x}_j$ is fitted by weighted least squares, and the SHARP rational filter removes coefficients with $|\beta_j| < \kappa \max_k |\beta_k|$ ($\kappa = 0.05$). Feature attributions are normalised:

$$\phi_j = \frac{|\beta_j|}{\sum_k |\beta_k|}.$$

17. Evaluation Metrics & Formal Definitions

Definition 17.1 (Structural Similarity Index (SSIM)). For image patches x and \hat{x} with means $\mu_x, \mu_{\hat{x}}$, variances $\sigma_x^2, \sigma_{\hat{x}}^2$, and covariance $\sigma_{x\hat{x}}$:

$$\text{SSIM}(x, \hat{x}) = \frac{(2\mu_x \mu_{\hat{x}} + C_1)(2\sigma_{x\hat{x}} + C_2)}{(\mu_x^2 + \mu_{\hat{x}}^2 + C_1)(\sigma_x^2 + \sigma_{\hat{x}}^2 + C_2)},$$

where $C_1 = (0.01 \cdot L)^2$ and $C_2 = (0.03 \cdot L)^2$ with L the dynamic range of pixel values.

Definition 17.2 (Normalised Mutual Information (NMI)).

$$\text{NMI}(Y, \hat{Y}) = \frac{2I(Y; \hat{Y})}{H(Y) + H(\hat{Y})},$$

where $I(Y; \hat{Y}) = H(Y) - H(Y|\hat{Y})$ is the mutual information and $H(\cdot)$ is the Shannon entropy. $\text{NMI} \in [0, 1]$; a value of 1 indicates perfect alignment.

Definition 17.3 (Demographic Bias Gap). For demographic groups $a_i, a_j \in \mathcal{A}$:

$$\Delta_{\text{bias}} = \max_{a_i, a_j \in \mathcal{A}} \|\mathbb{E}[G_\theta(z) | a_i] - \mathbb{E}[G_\theta(z) | a_j]\|_2.$$

18. Adam Optimiser & Convergence Bound

Theorem 18.1 (Adam Convergence in Non-Convex Settings). Let $\mathcal{L}_G : \Theta \rightarrow \mathbb{R}$ be β -smooth and lower

bounded. Under the Adam update rule (Equations 31–34 of the main text) with $\beta_1 = 0.9$, $\beta_2 = 0.999$, $\epsilon = 10^{-8}$, and learning rate $\eta_t = \eta/\sqrt{t}$, after T iterations:

$$\frac{1}{T} \sum_{t=1}^T \mathbb{E} \left[\|\nabla \mathcal{L}_G(\theta_t)\|^2 \right] \leq \mathcal{O} \left(\frac{\ln T}{\sqrt{T}} \right).$$

Proof Sketch. This follows from the analysis of Reddi et al. (2018) *On the Convergence of Adam and Beyond*. The adaptive step sizes $\eta/(\sqrt{\hat{v}_t} + \epsilon)$ are bounded above by η/ϵ , ensuring bounded updates. Telescoping the smoothness inequality and bounding the bias-correction terms introduces an additional $\ln T$ factor relative to SGD, yielding the $\mathcal{O}(\ln T/\sqrt{T})$ rate. AdamW further decouples weight decay from gradient scaling, improving the constant but not the asymptotic rate. \square